

# THESIS PROPOSAL

**Title:** Indirect measurement of cosmic-ray proton spectrum using Earth's  $\gamma$ -ray data from *Fermi* Large Area Telescope

**Student:** Patomporn Payoungkhamdee 6138171 SCPY/M

**Supervisor:** Assistant Professor Warit Mitthumsiri  
Professor David Ruffolo

**Degree:** Master's degree

**Field of study:** Physics

**Faculty of Science, Mahidol University**

## 1 Introduction

Cosmic-ray research has been pioneered by Theodor Wulf and Victor Hess who took electrometer measured cosmic rays from the ground to a higher altitude and later experiment has confirmed that there are a cosmic rays from outer space which can penetrate and interact with the Earth's atmosphere [1–3].

There are many possible phenomena of acceleration mechanism in the space that could produce high energy particles. Consequently, characteristic of acceleration mechanism could roughly be distinguished by a spectral index in the arrival of cosmic rays spectrum in rigidity. The breaking point of the spectrum mainly come from the overlapped region of acceleration mechanism that could be an evidence to explore a new candidate of cosmic ray source.

In 2011, PAMELA detector indicated that there is a breakpoint of cosmic-ray protons spectrum around 240 GV [4]. Furthermore, AMS-02 also found a drastic change of cosmic-ray proton spectrum at around 336 GV [5].

In this work, the indirect measurement of cosmic ray protons will be performed by using gamma-ray data from *Fermi* Large Area Telescope (*Fermi*-LAT).

## 2 Background knowledge

### 2.1 Cosmic rays

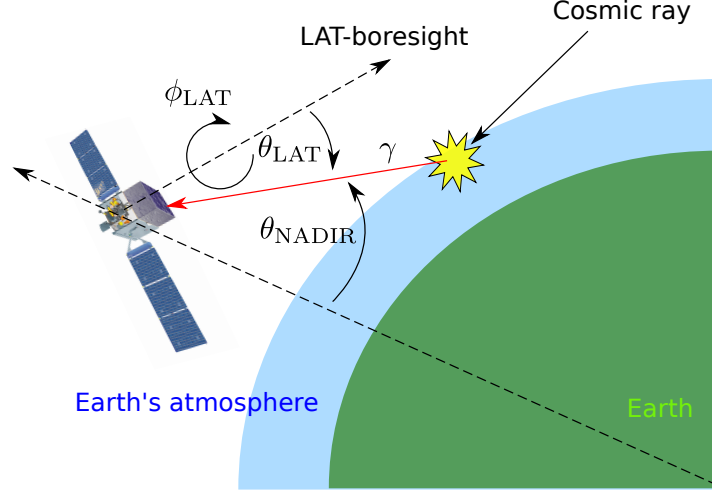


Figure 1: Schematic of  $\gamma$ -ray production

Cosmic rays (CRs) are high energy particles which are produced in space by various types of acceleration mechanisms such as supernovae, active galactic nuclei, quasars, and gamma-ray bursts. The main composition of CRs consist of 90% protons, 8% alpha and other heavier atoms. The widely accepted explanation of why CR spectrum follows a power-law function in rigidity is that the acceleration mechanism was modeled as a diffusive shock which has a characteristic spectral index.

The values of CR spectral indices vary for different ranges of energies, depending on the types of sources which can accelerate CRs to a certain energy range as shown in Figure 2 and Figure 3 [6].

The motivation why we use  $\gamma$ -ray as a secondary product for investigating incident proton spectrum is that Earth limb's  $\gamma$ -ray relatively brighter than the sky due to collision from CRs in energy range 100 MeV and 1 TeV which consistent with our study [7].

Previous work has been performed using Pass 7 version data [8] and found an energy breakpoint around 300 GeV with a significance level of around  $2\sigma$  [9]. This result agree to the direct measurements from [4, 5].

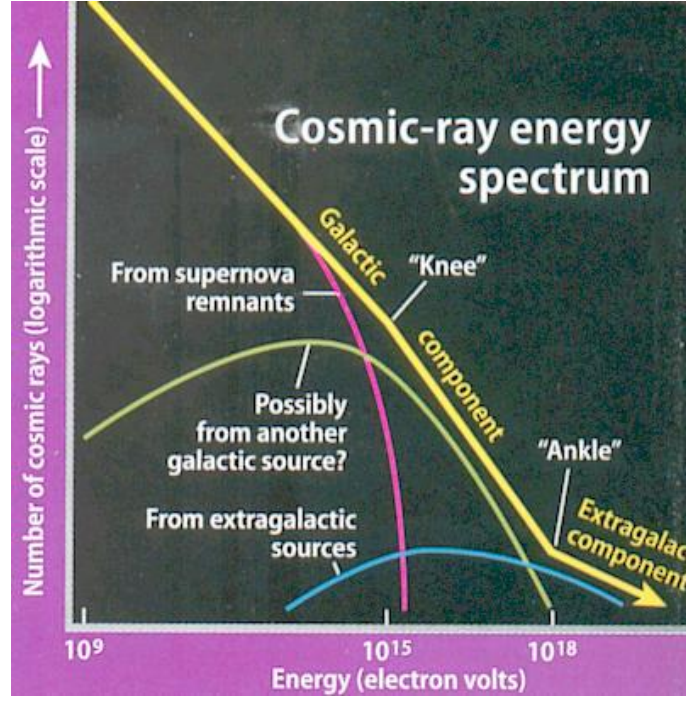


Figure 2: characteristic of CRs spectrum: Image taken from universe-review.ca

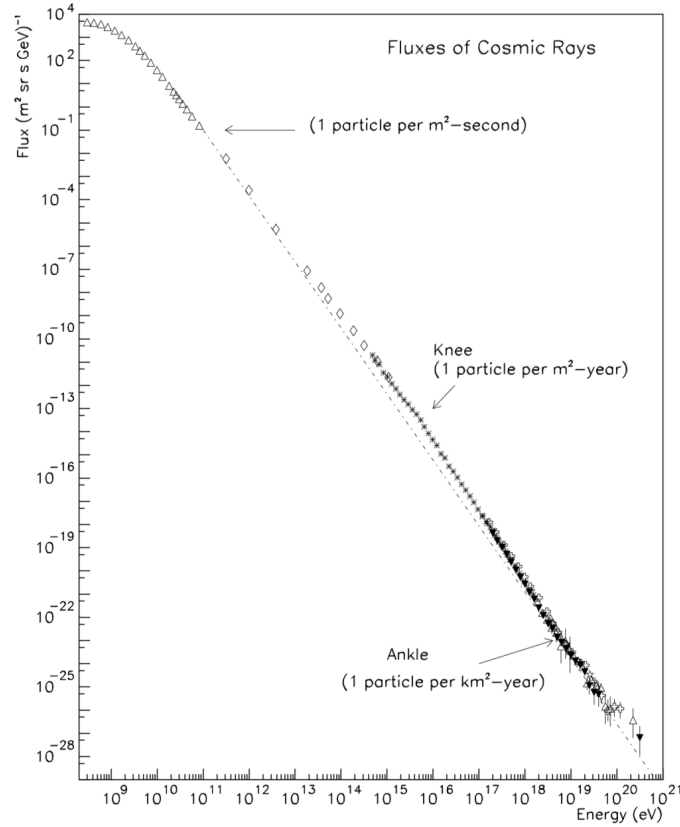


Figure 3: Observation of CRs spectrum: Image taken from Swordy [6]

## 2.2 *Fermi* Large Area Telescope

Gamma-ray Large Area Space Telescope (GLAST) could be informally called *Fermi*-LAT. The mission is to collect data of particles from multiple phenom-

ena such as active galaxy nuclei (AGN), pulsars and other high energy sources. It also attaches the Gamma-ray Burst Monitor (GBM) to study gamma-ray bursts. Fermi was launched on 11 June 2008 at 16:05 UTC aboard a Delta II 7920-H rocket.

## Instrument

LAT consists of 16 layers of tracker (TKR) modules, 16 calorimeters (CAL) and a partition Anti-Coincidence Detector (ACD).

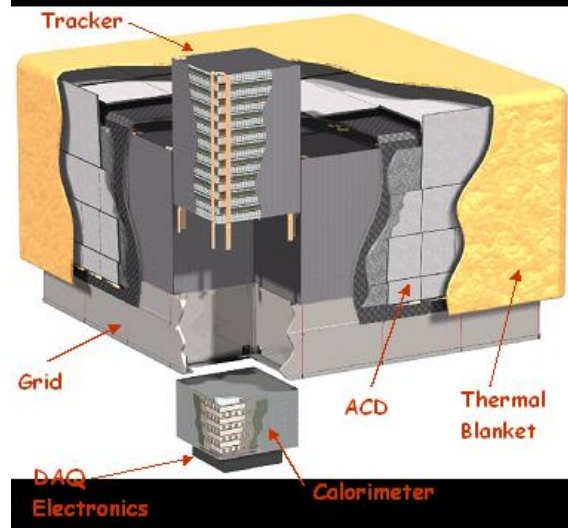


Figure 4: Instrument structure : Image taken from <https://fermi.gsfc.nasa.gov>

TKR module has made from an array of silicon-strip tracking detectors (SSDs) and has 18 trackers on a horizontal plane. First 12 planes have 0.035 radiation lengths, next 4 layers contain 0.18 radiation lengths thick and the rest of it does not have any converter. Tracking detectors in each plane consist of two planar inner layer which running in x and y axis subsequently. The arrival  $\gamma$ -ray in LAT's field of view could produce electron-positron pair in TKR's plates. The initial lepton pair could be determined from the record of conversion point in SSD planes with a power angular resolution when it has a low energy.

Each CAL module contains 1536 CsI(Tl) crystal with a 96 crystal align in eight different orthogonal layers. Dual PIN photodiodes also attach in each crystal which provides a great resolution in energy.

ACD tile contains wavelength shifting fiber by photomultiplier tubes (PMT) for avoding majority of incoming charged particles to prevent a veto signal in calorimeters which cause an inefficient of the instrument.

## Event reconstruction

The methodology of detection is to track a lepton pair product from an incident photon that collides with the conversion foil and lepton products be traced by the second inner layer of TKR. Consequently, the limit of precision depends on the energy of photon that larger than the rest mass energy of electron-positron as well as angle resolution of TKR that getting worse at larger  $\theta_{\text{LAT}}$ . Lastly, the energy of the lepton product could be captured by a precision crystal array in CAL. The event classification is divided into various levels of confident [10, 11].

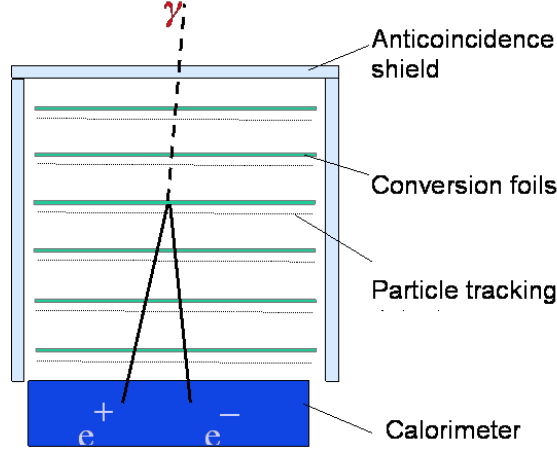


Figure 5: Structure of the LAT : Image taken from <https://fermi.gsfc.nasa.gov>

## 3 Methodology and Scope

### 3.1 Data sets

Photon data with a newest version of events reconstruction (would be last version) from *Fermi*-LAT

- P8R2\_ULTRACLEANVETO\_V6 data from 07/08/2008 to 16/10/2017 ( $\sim 9$  years)
- Collect photon energy range = 10 GeV to 1 TeV
- $\theta_{\text{NADIR}} = 68.4^\circ - 70^\circ$  (Earth's limb)
- Use  $\theta_{\text{LAT}} < 70^\circ$

Note that the reasons that we use ULTRACLEANVETO type of event reconstruction are it is the cleanest reconstruction catalogue.

### 3.2 Flux extraction

1. Make 2D histograms with 25 bins per decade of energy
2. Select photon data and fill in the 2D histograms
3. Calculate exposure maps which include the effective area and livetime of the LAT as it observed the Earth

$$\mathbf{Flux} \equiv \frac{dN_\gamma}{dE} = \frac{\int_{\text{Limb region}} (\text{Count map}/\text{Exposure map})}{\Delta\Omega\Delta E} \quad (1)$$

4. Taking consider background subtraction from a average uniform background photon distribution by treating bin by bin

### 3.3 Coordinate Transformations

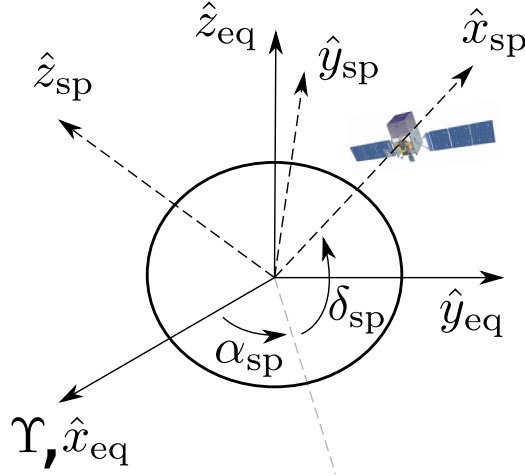


Figure 6: Coordinate transform between celestial and spacecraft

$$\begin{aligned} \hat{x}_{\text{sp}} &= \cos \delta_{\text{sp}} \cos \alpha_{\text{sp}} \hat{x}_{\text{eq}} + \cos \delta_{\text{sp}} \sin \alpha_{\text{sp}} \hat{y}_{\text{eq}} + \sin \delta_{\text{sp}} \hat{z}_{\text{eq}} \\ \hat{z}_{\text{sp}} &= -\sin \delta_{\text{sp}} \cos \alpha_{\text{sp}} \hat{x}_{\text{eq}} - \sin \delta_{\text{sp}} \sin \alpha_{\text{sp}} \hat{y}_{\text{eq}} + \cos \delta_{\text{sp}} \hat{z}_{\text{eq}} \\ \hat{y}_{\text{sp}} &= \hat{z}_{\text{sp}} \times \hat{x}_{\text{sp}} \end{aligned} \quad (2)$$

The transform matrix between equatorial coordinate and spacecraft coordinate could be represented as a relation in Eq 2

$$\hat{r}_{\text{sp}} \equiv T_{\text{eq} \rightarrow \text{sp}}(\delta_{\text{sp}}, \alpha_{\text{sp}}) \hat{r}_{\text{eq}} \quad (3)$$

$$\begin{aligned}
\hat{x}_p &= \cos \delta_p^x \cos \alpha_p^x \hat{x}_{eq} + \cos \delta_p^x \sin \alpha_p^x \hat{y}_{eq} + \sin \delta_p^x \hat{z}_{eq} \\
\hat{z}_p &= \cos \delta_p^z \cos \alpha_p^z \hat{x}_{eq} + \cos \delta_p^z \sin \alpha_p^z \hat{y}_{eq} + \sin \delta_p^z \hat{z}_{eq} \\
\hat{y}_p &= \hat{z}_p \times \hat{x}_p
\end{aligned} \tag{4}$$

According to Eq 4, the transformation matrix between LAT-boresight and equatorial coordinate could be derived from

$$\hat{r}_p \equiv T_{eq \rightarrow p}(\delta_p^x, \alpha_p^x, \delta_p^z, \alpha_p^z) \hat{r}_{eq} \tag{5}$$

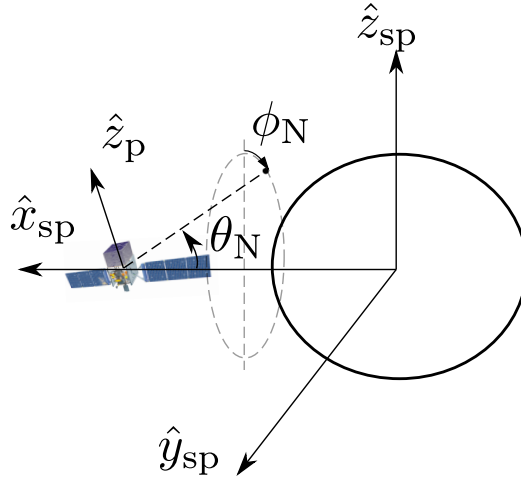


Figure 7: Coordinate transform between spacecraft and nadir angle

Importantly, the current status of lat field of view need to be consider in order to fill in the exposure map with the Earth's polar coordinate from satellite point of view as

$$\hat{r}_{sp}^o(\theta_N, \phi_N) \equiv -\cos \theta_N \hat{x}_{sp} + \sin \theta_N \cos \phi_N \hat{z}_{sp} + \sin \theta_N \sin \phi_N \hat{y}_{sp} \tag{6}$$

Since the spacecraft coordinate has already linked to the nadir's angle, the next step is to transform it into central coordinate which basically is the equatorial coordinate and convert it into LAT-boresight coordinate (Eq 7)

$$\hat{r}_p^o(\theta_N, \phi_N) = T_{eq \rightarrow p}(\delta_p^x, \alpha_p^x, \delta_p^z, \alpha_p^z) [T_{eq \rightarrow sp}(\delta_{sp}, \alpha_{sp})]^{-1} \hat{r}_{sp}^o(\theta_N, \phi_N) \tag{7}$$

Geometrically, angular coordinate of LAT plane could be obtained from normalized component of the cartesian unit vector as in Fig 8. The exposure accumulation has been calculated in every single grid from the previous relation.

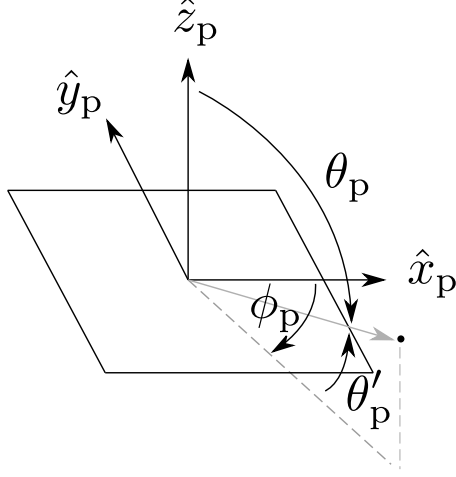


Figure 8: Detector's boresight in cartesian and polar coordinate

The calculation of exposure map has to be done wisely one energy at a time due to the effective area of the spacecraft at each angle has various efficiency depends on the incident energy of gamma-ray as in the Fig 9. Under the condition of exposure-energy at a time, another factor that has to be considered carefully is the resolution of the exposure map. The higher resolution, the longer calculation time consumption which means we have to make  $\theta_N$  more precise than  $\phi_N$  because the limb region is more sensitive.

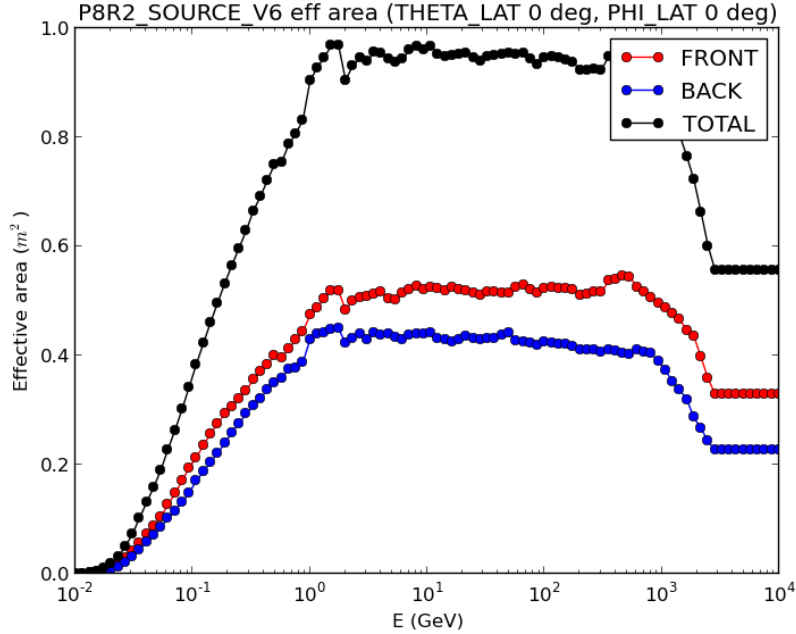


Figure 9: Effective area of Fermi-LAT

For both reasons, the first version of calculation takes approximately a



month or more to finish. However, there is a plenty of room to improve. Here is why parallel computation fit really well to this problems. To maximize all of the threading process in the cluster, master-slave technique has been applied to get rid of the idle thread to maximize our resource of computation.

### 3.4 Interaction model

Incident proton spectrum in rigidity be represented as  
**Single power law (SPL)**

$$\frac{dN}{dR} = R_0 R^{-\gamma} \quad (8)$$

**Broken power law (BPL)**

$$\frac{dN}{dR} = \begin{cases} R_0 R^{-\gamma_1} & : E < E_{\text{Break}} \\ R_0 [R(E_{\text{Break}})]^{\gamma_2 - \gamma_1} R^{-\gamma_2} & : E \geq E_{\text{Break}} \end{cases} \quad (9)$$

In this work, we use the scattering amplitude from hadronic collision [12] that could produce a photon as a secondary product that could be detected by *Fermi*-LAT.

$$\frac{dN_\gamma}{dE_\gamma} \propto \int_{E_\gamma}^{E_{\text{max}}} dE' \frac{dN_p}{dE'} \frac{d\sigma^{pp \rightarrow \gamma}(E', E_\gamma)}{dE_\gamma} \quad (10)$$

The atmospheric composition already known well enough that mostly combined with nitrogen gas as well as oxygen molecules [13]. In order to get scattering amplitude from proton-proton collision we treat a crossection of single hadronic collision with a fraction of nitrogen atom which is almost equal to oxygen atom [14] at relativistic level of kinetic energy.

In 2015, the direct measurement of Helium specrtum has been done by using AMS-02 in [15]. Improvement of model precision was included by taking into account incident of Helium cosmic ray particle as a first order correction and please note that we ignore other heavier atom.

$$\frac{dN_\gamma}{dE_\gamma}(E_\gamma) \propto \sum_{E_{\text{inc},i}} \left[ \frac{E_{\text{inc},i}}{E_\gamma} \Delta(E_{\text{inc},i}) \right] \left[ f_{pp} \frac{dN_{\text{H}}}{dE_{\text{inc}}}(E_{\text{inc},i}) \left\{ 1 + \frac{\sigma_{\text{HeN}}}{\sigma p N} \left( \frac{dN_{\text{H}}}{dR} \right)^{-1} \frac{dN_{\text{He}}}{dR} \frac{dR_{\text{He}}}{dR_{\text{H}}} \right\} \right] \quad (11)$$

where

- Red color terms is an **incident proton spectrum** as in Eq (8, 9)
- Use **helium spectrum from AMS-02 measurement (2015)**

- $f_{pp} \equiv E_\gamma(d\sigma^{ij \rightarrow \gamma}/dE_\gamma)$  is a table in K&O model which behave like a scattering amplitude that depend on the energy of incident particle
- Crosssection  $\sigma_{\text{HeN}}/\sigma_{pN}$  at energy more than 10 GeV is approximately plateau ( $\approx 1.6$ )

### 3.5 Optimization

**Poisson likelihood function** define as Eq 12

$$\mathcal{L} = \prod_{i=1}^N P_{\text{pois}}(n_{i,\text{model}}, n_{i,\text{measurement}}) \quad (12)$$

Since our spectrum order is in different order of magnitude, then the better way to define an objective function is to redefine a likelihood as a log-likelihood function for numerically convenient like Eq 13.

$$\text{Sum} = \sum_{i=1}^N -\log P_{\text{pois}}(n_{i,\text{model}}, n_{i,\text{measurement}}) \quad (13)$$

In order to get a best fit spectral indices, we do an optimization with a proper trial parameters for take gradient descent from Poisson loss function between model spectrum and flux from measurement as Figure 10

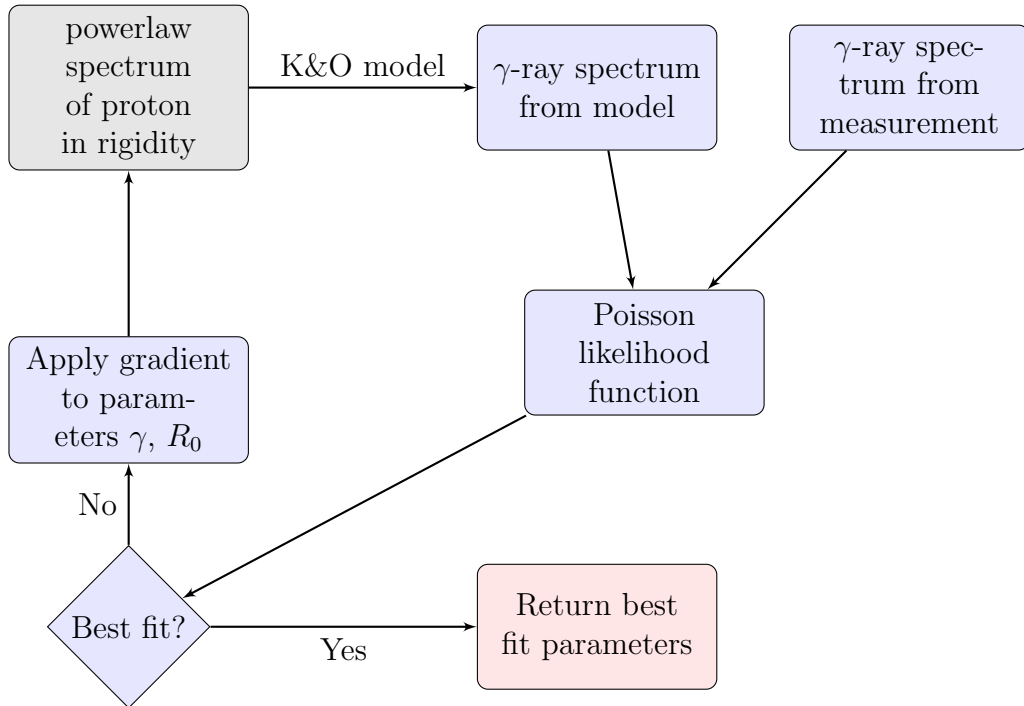


Figure 10: Flow chart of optimization process

### 3.6 Monte Carlo Simulation

In this section, we perform a brute force method to find an error of any parameters (spectral indices and break point energy). For a **statistical error (random error)**, we rerandom a counts on each bin by poisson random generator and recalculate the flux after that optimize it as the Fig 10 do. The process of this algorithm has shown in Fig 11. The amount of simulation process require an enough number of sampling to fill up the optimized parameters and see the shape of gaussian distribution curve looks obvious enough which our work done is roughly 2000 sampling.

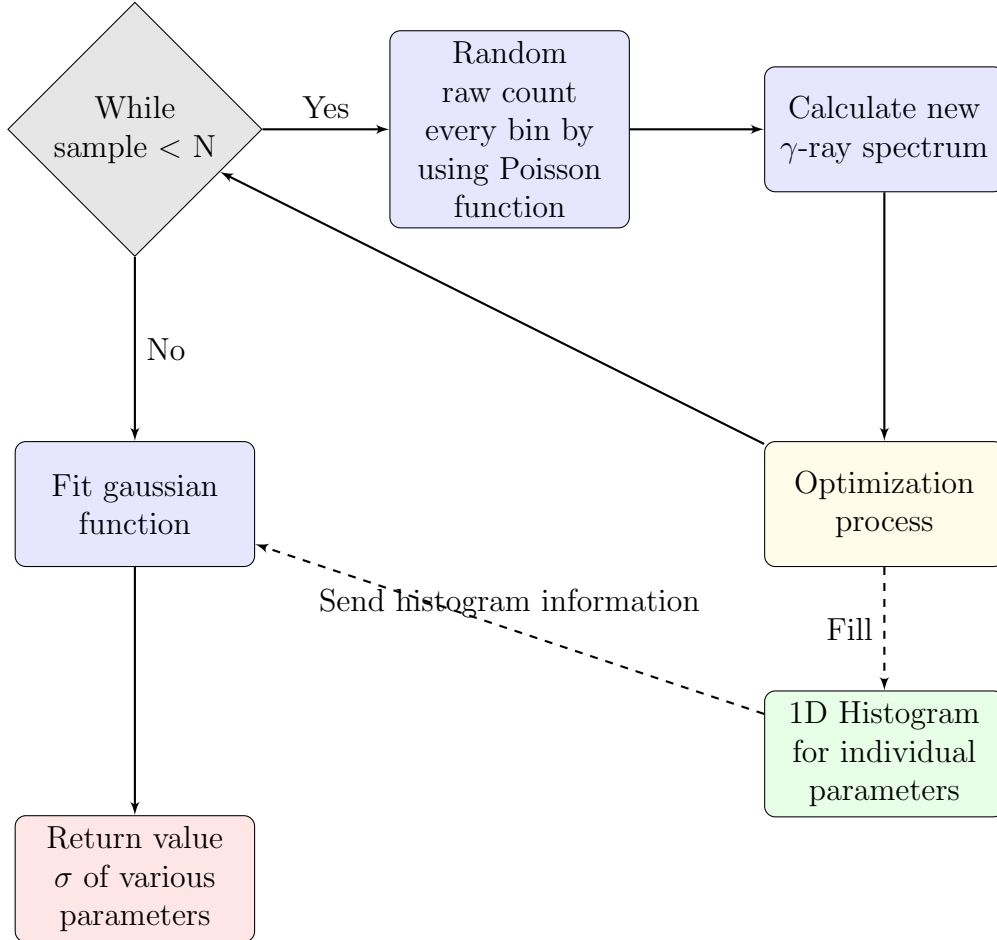


Figure 11: Flow chart of Monte Carlo simulation for statistical error

For **total error**, we also take into account error from instrument which is LAT that depends on energy. We exactly the same as the statistical error determination but one more thing that including to this algorithm is to pick three energy bin (10, 100, 1000 GeV) then rerandom flux in these three bin and apply a cubic spline interpolation to smooth the line for a statistical reason [10]. The demonstration of this program is shown as Fig 12.

### 3.7 Likelihood ratio test (LRT)

In order to determine significant level between null model and alternative model, we use Wilk's theorem [16]. Basically, this method is to regard a given likelihood

$$\mathcal{L} \equiv \prod_{\alpha=1}^n f(x_{\alpha}, \theta_1, \theta_2, \dots, \theta_h) \quad (14)$$

where

- $x_{\alpha}$  is represent a variant from model and data
- $\theta_i$  is a degree of freedom (DOF)

The explicit declaration with an obvious method to implement has been proved in [17] as the Eq 15

$$\text{LRT} = -2 \ln \left( \frac{\mathcal{L}_{\text{null}}}{\mathcal{L}_{\text{alternative}}} \right) \quad (15)$$

## 4 Preliminary Results

### Count map and distribution

First step to check whether data that have in our hand is makes some sense or not is to simply plot the distribution of photon from a picked single weekly photon file as in Fig 13. Another step is to see the histogram of photon over energy as 14.

### Exposure maps

This step require a lot of effort to make it robust and many of testing has been performed from the serial to parallel code along the way of development. To overview some of the exposure map, the selected four out of fifty exposure map has shown in the Fig (15, 16) in cartesian and polar plot sequentially.

### Differential Flux of $\gamma$ -ray

Lastly, preliminary of gamma-ray spectrum has been computed and show in Fig 17.

## 5 Research planning

Task\Timing	Jan 2020	Feb 2020	Mar - July 2020	Aug 2020
Extract limb's gamma-ray				
Statistical Testing				
SPC 2020				
Writing Thesis				
Thesis Defense				

Table 1: Timeline

## 6 Outlook

- Find a breaking point of cosmic ray proton spectrum and determine level of confidence
- Put weight on the previous study that the brightness of  $\gamma$ -ray from Earth's high atmosphere could be used to perform an indirect measurement

## References

- [1] V. F. Hess (The Nobel Foundation, 1936).
- [2] D. Pacini, Il Nuovo Cimento **3**, 93 (1912), URL <https://doi.org/10.1007/BF02957440>.
- [3] J. Clay, Proceedings of the Section of Sciences, Koninklijke Akademie van Wetenschappen te Amsterdam **30**, 1115 (1927).
- [4] O. Adriani, G. C. Barbarino, G. A. Bazilevskaya, R. Bellotti, M. Boezio, E. A. Bogomolov, M. Bongi, V. Bonvicini, S. Borisov, S. Bottai, et al., The Astrophysical Journal **765**, 91 (2013), URL <http://stacks.iop.org/0004-637X/765/i=2/a=91>.
- [5] M. Aguilar (AMS Collaboration), Phys. Rev. Lett. **114**, 171103 (2015), URL <https://link.aps.org/doi/10.1103/PhysRevLett.114.171103>.
- [6] S. Swordy, Space Science Reviews **99**, 85 (2001), ISSN 1572-9672, URL <https://doi.org/10.1023/A:1013828611730>.
- [7] A. A. Abdo, M. Ackermann, M. Ajello, W. B. Atwood, L. Baldini, J. Ballet, G. Barbiellini, D. Bastieri, B. M. Baughman, K. Bechtol, et al. (Fermi-LAT Collaboration), Phys. Rev. D **80**, 122004 (2009), URL <https://link.aps.org/doi/10.1103/PhysRevD.80.122004>.

- [8] M. Ackermann, M. Ajello, A. Albert, A. Allafort, W. B. Atwood, M. Axelsson, L. Baldini, J. Ballet, G. Barbiellini, D. Bastieri, et al., The Astrophysical Journal Supplement Series **203**, 4 (2012), URL <http://stacks.iop.org/0067-0049/203/i=1/a=4>.
- [9] M. Ackermann, M. Ajello, A. Albert, A. Allafort, L. Baldini, G. Barbiellini, D. Bastieri, K. Bechtol, R. Bellazzini, R. D. Blandford, et al. (Fermi LAT Collaboration), Phys. Rev. Lett. **112**, 151103 (2014), URL <https://link.aps.org/doi/10.1103/PhysRevLett.112.151103>.
- [10] M. Ackermann, M. Ajello, A. Albert, A. Allafort, W. B. Atwood, M. Axelsson, L. Baldini, J. Ballet, G. Barbiellini, D. Bastieri, et al., The Astrophysical Journal Supplement Series **203**, 4 (2012), URL <http://stacks.iop.org/0067-0049/203/i=1/a=4>.
- [11] W. Atwood et al. (Fermi-LAT) (2013), 1303.3514, URL <http://inspirehep.net/record/1223837/files/arXiv:1303.3514.pdf>.
- [12] M. Kachelrieß and S. Ostapchenko, Phys. Rev. D **86**, 043004 (2012), URL <https://link.aps.org/doi/10.1103/PhysRevD.86.043004>.
- [13] J. M. Wallace and P. V. Hobbs, *Atmospheric* (Science, 2006).
- [14] T. W. Atwater and P. S. Freier, Phys. Rev. Lett. **56**, 1350 (1986), URL <https://link.aps.org/doi/10.1103/PhysRevLett.56.1350>.
- [15] M. Aguilar, D. Aisa, B. Alpat, A. Alvino, G. Ambrosi, K. Andeen, L. Arruda, N. Attig, P. Azzarello, A. Bachlechner, et al. (AMS Collaboration), Phys. Rev. Lett. **115**, 211101 (2015), URL <https://link.aps.org/doi/10.1103/PhysRevLett.115.211101>.
- [16] S. S. Wilks, Ann. Math. Statist. **9**, 60 (1938), URL <https://doi.org/10.1214/aoms/1177732360>.
- [17] J. P. Huelsenbeck and K. A. Crandall, Annual Review of Ecology and Systematics **28**, 437 (1997), <https://doi.org/10.1146/annurev.ecolsys.28.1.437>, URL <https://doi.org/10.1146/annurev.ecolsys.28.1.437>.

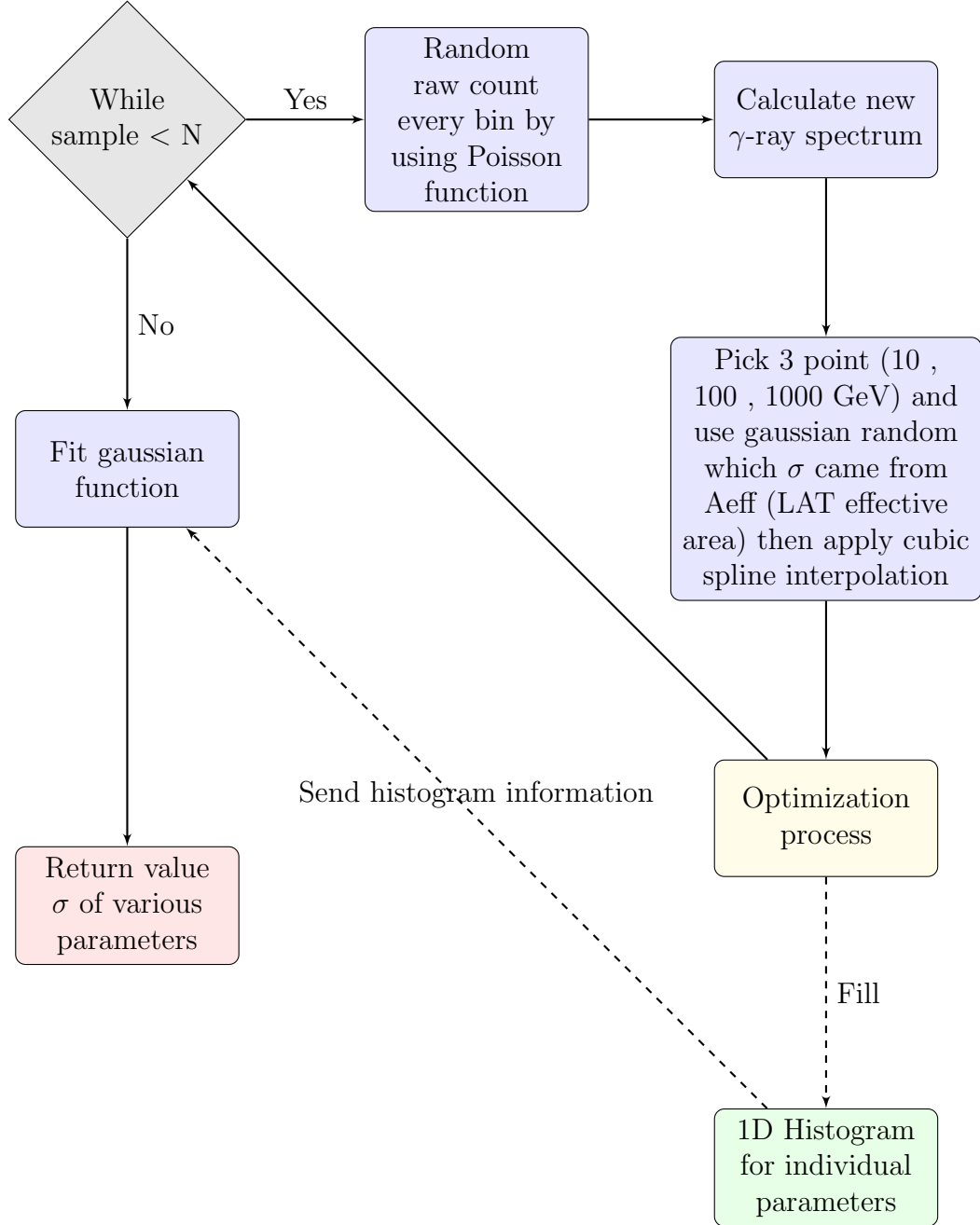


Figure 12: Flow chart of Monte Carlo simulation for total error

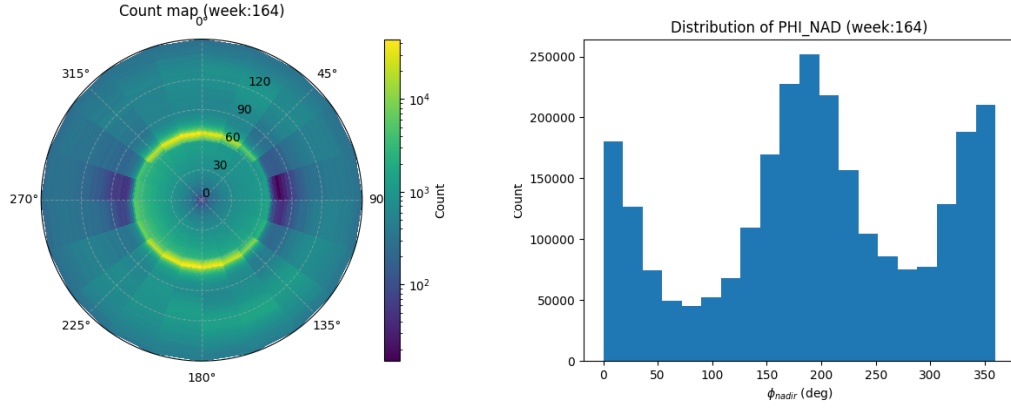


Figure 13: An example distribution of  $\gamma$ -ray from a single week

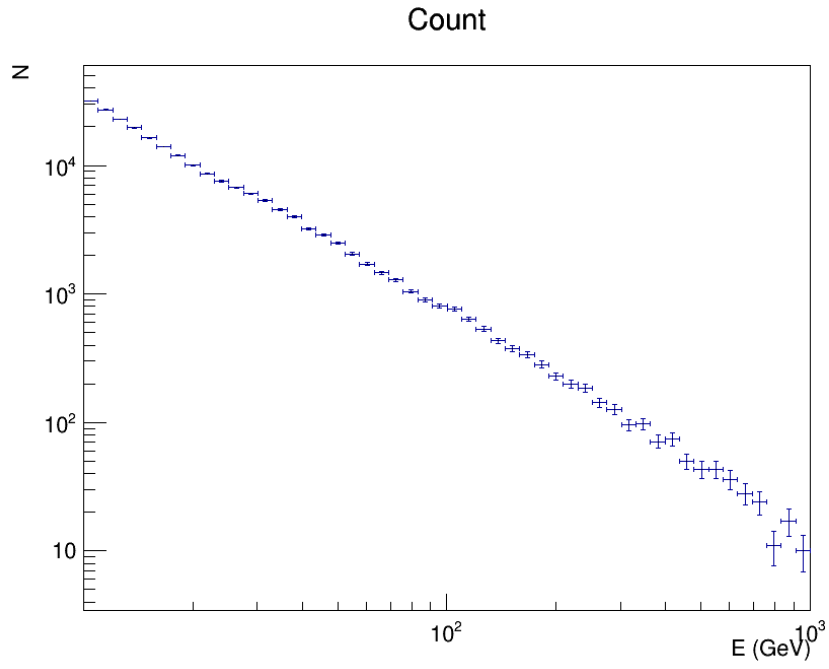


Figure 14: Raw histogram of photon in energy



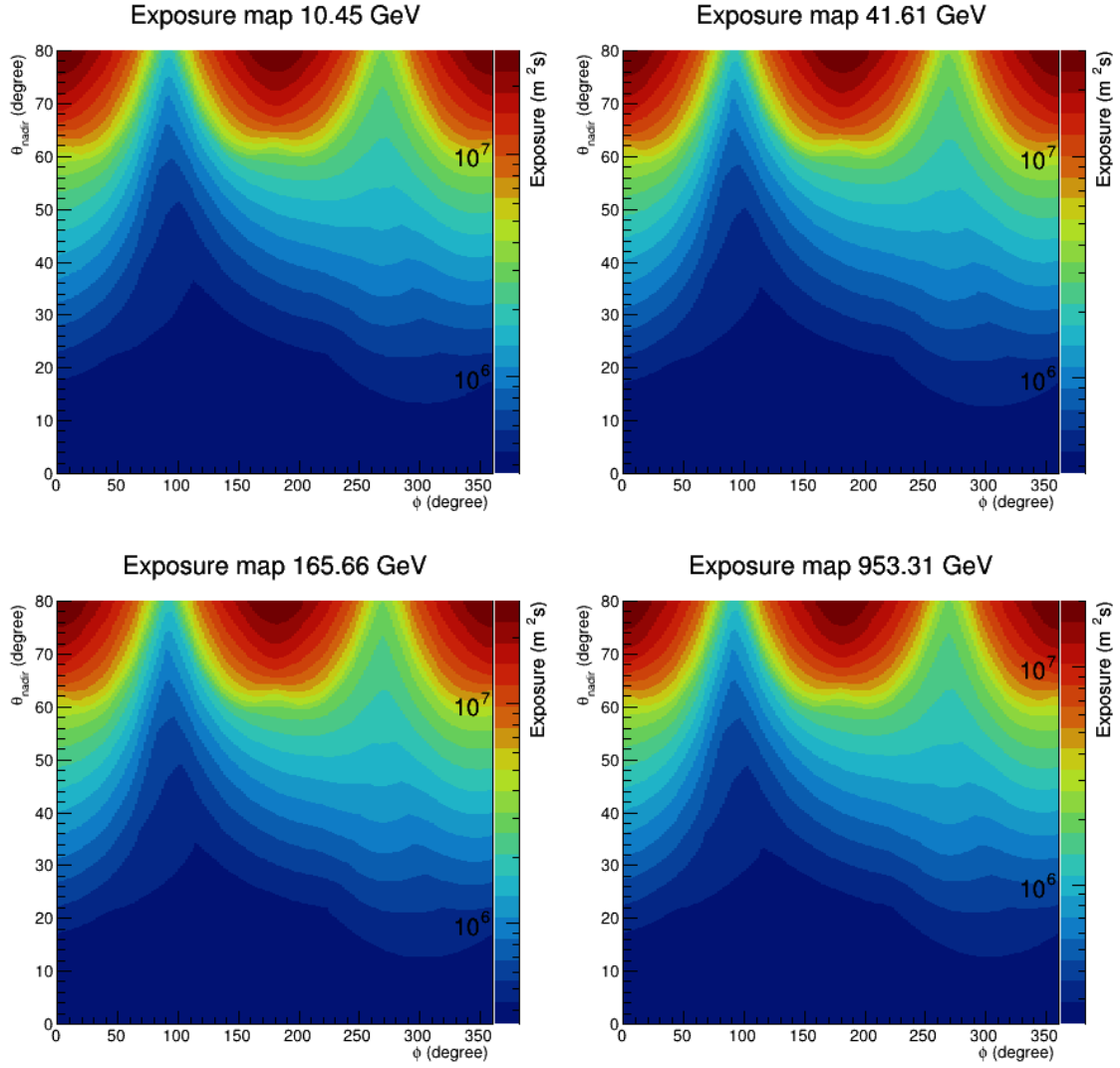


Figure 15: Exposure map of various  $\gamma$ -ray energy in cartesian plot

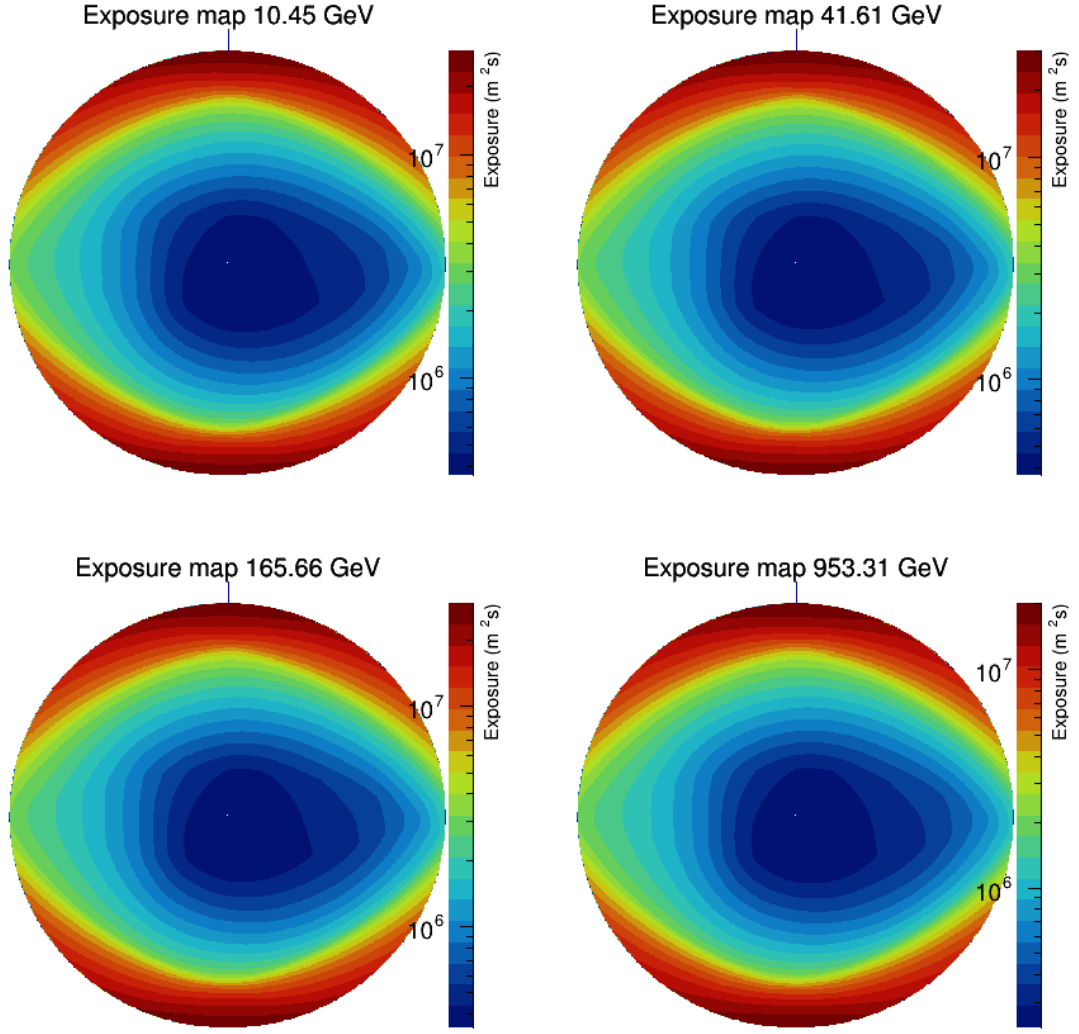


Figure 16: Exposure map of various  $\gamma$ -ray energy in polar plot

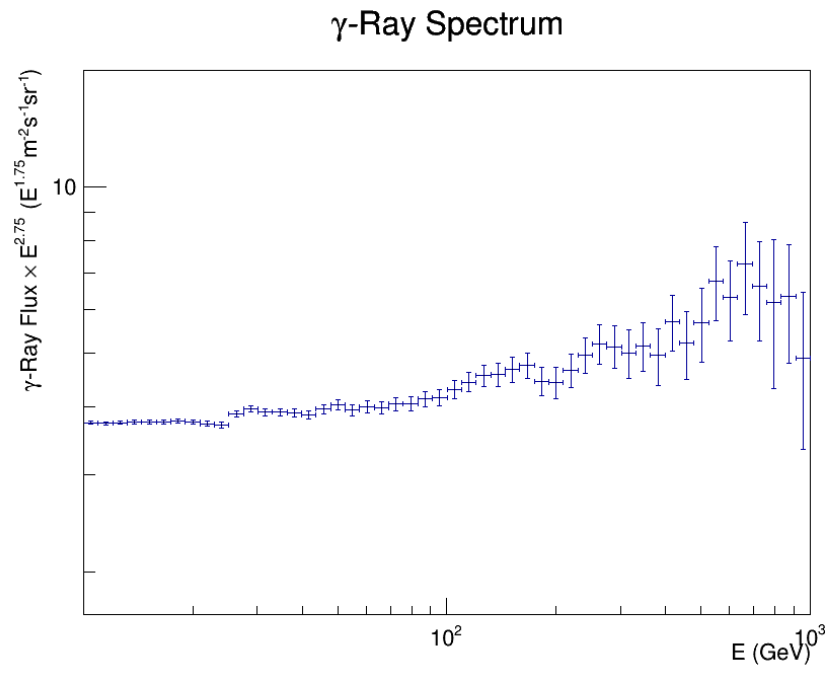


Figure 17:  $\gamma$ -ray spectrum in energy